Structural analysis of hypocentral distribution of an earthquake sequence using anisotropic wavelets: Method and application

Philippe Gaillot, José Darrozes, Pierre Courjault-Radé

▶ **To cite this version:**

Philippe Gaillot, José Darrozes, Pierre Courjault-Radé. Structural analysis of hypocentral distribution of an earthquake sequence using anisotropic wavelets: Method and application. Journal of Geophysical Research : Solid Earth, 2002, 107, 10.1029/2001JB000212 . insu-03642960

HAL Id: insu-03642960

https://insu.hal.science/insu-03642960

Submitted on 20 Apr 2022

HAL is a multi-disciplinary open access archive for the deposit and dissemination of scientific research documents, whether they are published or not. The documents may come from teaching and research institutions in France or abroad, or from public or private research centers.

L'archive ouverte pluridisciplinaire **HAL**, est destinée au dépôt et à la diffusion de documents scientifiques de niveau recherche, publiés ou non, émanant des établissements d'enseignement et de recherche français ou étrangers, des laboratoires publics ou privés.

Copyright

Structural analysis of hypocentral distribution of an earthquake sequence using anisotropic wavelets: Method and application

P. Gaillot[1]

Ecole et Observatoire des Sciences de la Terre, Institut de Physique du Globe de Strasbourg, Imagerie Tectonique, Strasbourg, France

UMR 5563, CNRS, Observatoire Midi Pyrénées, Université Paul Sabatier, Toulouse, France

J. Darrozes and P. Courjault-Radé

UMR 5563, CNRS, Observatoire Midi Pyrénées, Université Paul Sabatier, Toulouse, France

D. Amorese

UMR 6143 "M2C," CNRS, Centre de Géomorphologie, Université de Caen, Caen, France

Received 19 September 2000; revised 11 July 2001; accepted 22 August 2001; published 10 October 2002.

[1] Spatial organization of earthquake sequences is investigated to localize active rupture planes and to reconstruct the geometry of the inferred rupture zone. We have developed a new approach, the Normalized Optimized Anisotropic Wavelet Coefficient (NOAWC) method, to extract from a set of hypocenters the active ruptures planes. Our approach permits the detection of organized structures within a plane regardless of its size, location, shape anisotropy, and orientation. It includes the determination of a system of three perpendicular sections, minimizing the effects of projections of the hypocenters, and intrinsically accounts for uncertainty in the location of the seismic events. The accuracy and the effectiveness of the NOAWC procedure are illustrated on both synthetic and real data. An application to the $M = 5.1$ Arudy (French Pyrenees) aftershock sequence shows how a combination of the possible mathematically reconstructed geometries can be combined with the available fault plane solutions and geomorphological markers to determine the active rupture planes and to propose and validate a local tectonic model. This new multitool approach lends itself to quantitative and computer-assisted analyses of large data sets. *INDEX TERMS:* 7230 Seismology: Seismicity and seismotectonics; 8010 Structural Geology: Fractures and faults; 8107 Tectonophysics: Continental neotectonics; *KEYWORDS:* Multiscale analysis, wavelet, earthquakes, seismotectonics

Citation: Gaillot, P., J. Darrozes, P. Courjault-Radé, and D. Amorese, Structural analysis of hypocentral distribution of an earthquake sequence using anisotropic wavelets: Method and application, *J. Geophys. Res.*, *107*(B10), 2218, doi:10.1029/2001JB000212, 2002.

1. Introduction

[2] The characterization of active faults is of great interest for understanding the tectonic pattern and assessing the seismic risk within a given region. Seismogenic faults can be described by (1) geological mapping of their surface exposure, (2) determination of fault plane solutions of seismic events, and (3) identification of linear features in plots of hypocentral locations.

[3] The first two approaches have strong limitations: (1) Surface mapping of a fault trace cannot describe changes in fault geometry at depth nor localize subsurface fractures parallel (or subparallel) to the fault traces, (2) computation of fault plane solutions provides the fault geometry but cannot unequivocally identify the active fault plane without additional information, and, on the other hand, (3) the analysis of the spatial distribution of seismic events can contribute significantly to the understanding of active faults. Earthquake sequences are usually distributed in linear patterns; however, uncertainties on their locations and misinterpretation of events along nonparallel structures complicate the identification of rupture planes. A more reliable analysis of the spatial distribution of hypocenters requires the use of specific mathematical methods.

[4] Since 1965, several studies have discussed the analysis of spatial patterns within hypocenter or epicenter data sets. The spatial layout of events has been evaluated by the distribution of nearest-neighbor distances [*Suzuki and Suzuki*, 1965], the analysis of the number of events per unit area [*Suzuki and Suzuki*, 1966; *Chapman et al.*, 1997; *Amorese et al.*, 1999], the analysis of second- and higher-order moments of various catalogues [*Vere-Jones*, 1978; *Kagan*, 1981a, 1981b; *Kagan and Knopoff*, 1981; *Reasenberg*, 1985; *Fehler et al.*, 1987; *Eneva and Pavlis*, 1988], the measure of the

[1]Now at UMR 5568, CNRS, Laboratoire de Géophysique et Hydrodynamique de Forage, Université de Montpellier 2, Montpellier, France.

Copyright 2002 by the American Geophysical Union.
0148-0227/02/2001JB000212$09.00

degree of clustering or isolation of groups of seismic events using single-link cluster analysis [*Frolich and Davis*, 1990], and the recognition of fractal hierarchy via box-counting algorithms [e.g., *Robertson et al.*, 1995]. The determination of statistical parameters (usually dependent on magnitude) is also estimated for various statistical models of spatial and temporal influence [*Kagan and Knopoff*, 1976, 1978; *Prozorov and Dziewonski*, 1982; *Ouchi and Uekawa*, 1986].

[5] Most of the above methods analyze the spatial statistical distribution of earthquakes except the collapse method [*Jones and Stewart*, 1997] and the blade method [*Amorese et al.*, 1999]. As an improvement of the latter geometrical approach, we propose here an adaptative means of investigation related to the local geometry depicted by the distribution of earthquakes. This new procedure, the Normalized Optimized Anisotropic Wavelet Coefficient (NOAWC) method, is based on the wavelet transform that has already been applied to study the multiscale behavior of fracture networks [*Ouillon et al.*, 1995, 1996] and earthquake catalogues [*Bethoux et al.*, 1998]. For earthquake sequences the local and multiscale wavelet properties enable detection and quantification of clusters of seismic events regardless of their location, scale, and orientation. The significance of these clusters is examined. Combined with fault plane solutions and tectonic, or geomorphologic, evidence, some of these clusters can be interpreted in terms of rupture plane and hence allow reconstruction of the geometry of the inferred rupture zone.

2. Two-Dimensional Wavelet Transform and NOAWC Method

[6] The spatial distribution of seismic events is three-dimensional (3-D). However, a combination of 2-D map view and depth cross sections is used in practice to analyze the 3-D spatial distribution of the aftershocks and relate it to the main shock rupture surface and surface features [e.g., *Hauksson et al.*, 1995]. The wavelet transform (WT) efficiently performs the multiscale analysis of such 2-D images [*Antoine et al.*, 1993]. Several theoretical developments have shown the mathematical effectiveness [e.g., *Chui*, 1992; *Daubechies*, 1992] and the wide range of application of the WT formalism (see review by *Meyer and Roques*, 1993]).

3. Wavelet Transform Formalism

[7] Two-dimensional multiscale analysis by anisotropic wavelet transform consists of transforming a binary image through filters called wavelets [e.g., *Hagelberg and Helland*, 1995; *Escalera and MacGillivray*, 1995; *Ouillon et al.*, 1995]. The filters must have a zero mean (admissibility condition) and "sufficient" localization or decay in both spatial and frequency domains [*Chui*, 1992; *Daubechies*, 1992]. In this study, the anisotropic filters characterized by their aspect ratio (σ) are based on the Anisotropic Mexican Hat mother function, i.e., the second derivative of a Gaussian, allowing a great diversity in shape exploration [*Ouillon et al.*, 1995]:

$$\Psi_\sigma(\mathbf{x}) = \Psi_\sigma(x,y) = \left(2 - \frac{x^2}{y^2} - y^2\right) \exp\left[-\frac{1}{2}\left(\frac{x^2}{y^2} + y^2\right)\right], \quad (1)$$

where x and y are the Cartesian coordinates of each pixel.

[8] Each filter is characterized by four variables (a, **b**, σ, θ) that allow, for a given spatial resolution and a given location, the detection of anisotropic structures and singularities in any direction (Figure 1): a is the spatial resolution, i.e., the half short axis of the positive part of the wavelet for multiscale analysis by dilatation/contraction (the resolution is not a parameter of the method; in a practical manner, the resolution may be chosen as $a = (2m)$ (where $m = 1, 2, 3, \ldots, 10$) to respect the hierarchy that may exist between different classes of structures [*Escalera and McGillivray*, 1995]; each time, necessary, intermediate values can be used, e.g., to precise the scale of a given organization [*Gaillot et al.*, 1997]); **b** is the translation vector, i.e., the location of the filter on the image for local analysis (the translation vector covers the entire image); σ is the aspect ratio of the wavelet filter for

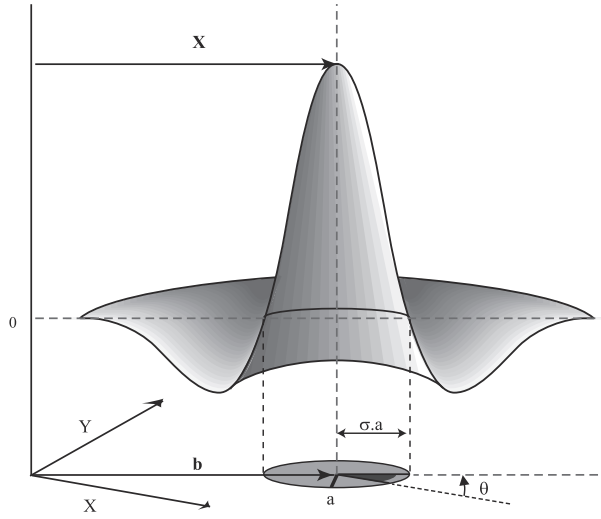

Figure 1. Schematic cross section of an anisotropic wavelet filter ψ(a, **x**, σ, θ). Parameters are location (**x**), resolution (a), shape ratio (σ), and orientation (θ) in the Cartesian coordinate system (X, Y); the detected entity is represented by an ellipse having the same parameters as the wavelet filter: location (**b**), half short axis (a), half long axis (σa), and azimuth of the long axis (θ).

Figure 2. (opposite) Representations of the local and multiscale properties of the wavelet transform coefficient. Computation of the wavelet coefficient of a signal $I(\mathbf{x})$ with the wavelet ψ(a, **x**, σ, θ) of resolution (a), location (**x** = **b**), shape anisotropy (σ), and elongation (θ) depends on the signal in the vicinity of (**b**) at the given spatial resolution. (a) $I(\mathbf{x})$ = const; a, **b**; (b) $I(\mathbf{x})$ not centered in **b**, (c) $I(\mathbf{x}) \approx 2a$; (c) $I(\mathbf{x}) > 2a$, **b**; (d) $I(\mathbf{x}) < 2a$, **b**; (e) $I(\mathbf{x}) \approx 2a$ and **x** = **b** ($I(\mathbf{x})$ is a group of objects (seismic events)); (f) $I(\mathbf{x}) \approx 2a$ and **x** = **b** ($I(\mathbf{x})$ is an unique entity); and (g) frequency distribution histogram (logarithmic scale) of a given NOAWC map. The slope break (T) between the few high coefficients and the lower coefficients is marked by an arrow. Letters refer to Figures 2a– 2f. Extraction of the wavelet parameters associated to the highest coefficients allows automatic representation of the significant lineaments.

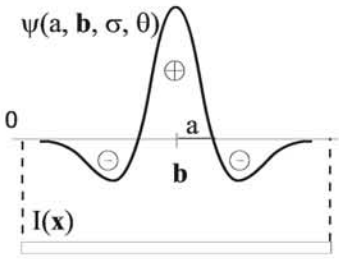

a

Null Wavelet Coefficient

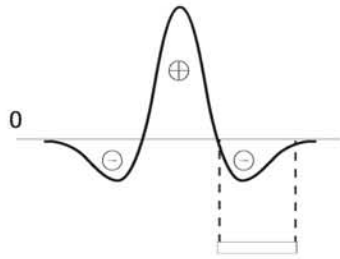

b

Negative Wavelet Coefficient

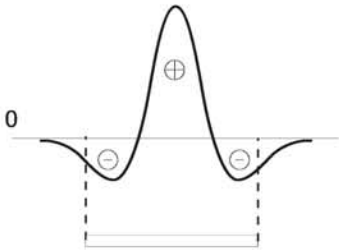

c

Weak Wavelet Coefficient

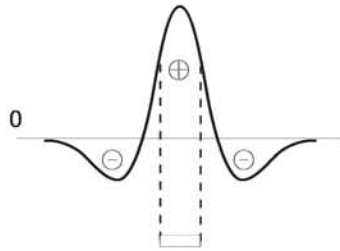

d

Weak Wavelet Coefficient

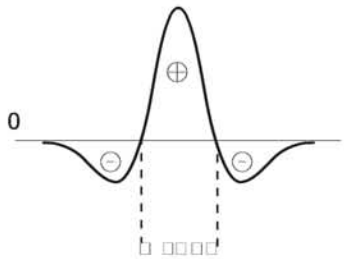

e

Strong Wavelet Coefficient

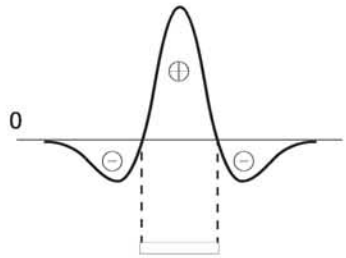

f

Maximum Wavelet Coefficient

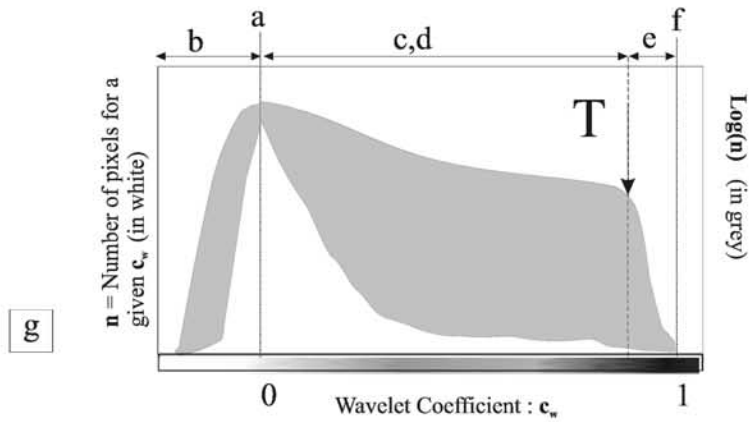

g

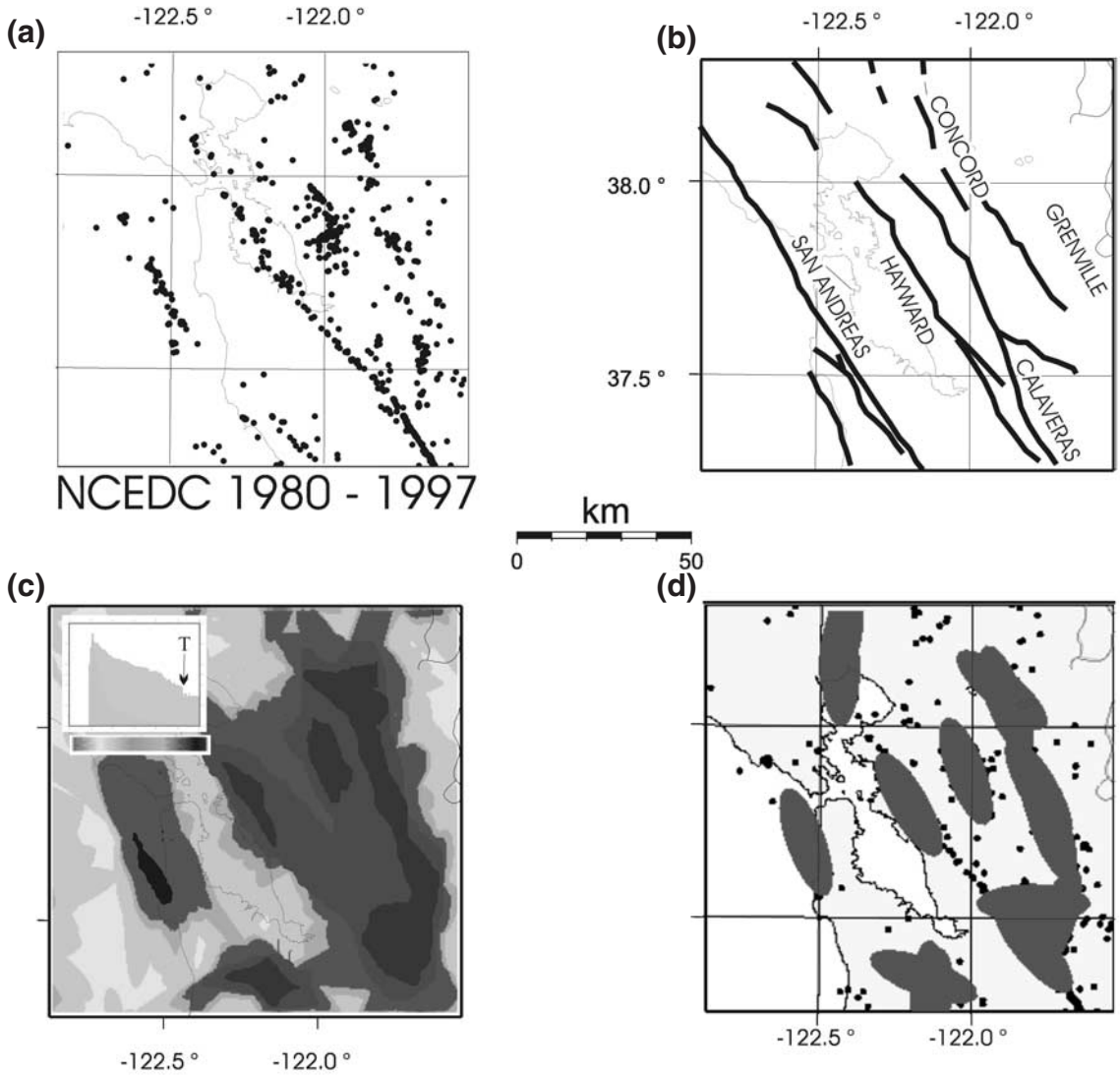

Figure 3. Two-dimensional illustration of San Francisco Bay area (121.53°W to 122.87°W, 37.25°N to 38.32°N). (a) Map of the 2228 epicenters (data from NCEDC, 1 January 1980 to 31 December 1997). (b) Mapped faults from *Castillo and Ellsworth* [1993]. (c) NOAWC map obtained for a resolution equal to the mean estimated error on location (a = 8 pixels $\sim$ 4 km). Low coefficients are white; high coefficients are black. Long axis of the wavelets associated with the selected local maxima ($T \approx 0.60$) is plotted (thin line). (d) Detected structures with their uncertitude envelope. The seismically active parts of the San Andreas, Calaveras, Hayward, Concord, and Greenville faults are detected. E-W alignments have also been evidenced and correspond to ''extra lines'' in respect to mapped faults.

shape recognition (the shape parameter is in between a and the image size); and θ is the azimuth of the long axis of the wavelet for angular exploration.

[9] The wavelet transform of an image is the convolution of the image $I(\mathbf{x})$ with a given analyzing filter $\psi(a, \mathbf{x}, \sigma, \theta)$. It transforms the image into a set of wavelet coefficients $C_I(a, \mathbf{x}, \sigma, \theta)$ displayed in a ''coefficient map.''

$$C_I(a, \mathbf{x}, \sigma, \theta) = \psi(a, \mathbf{x}, \sigma, \theta) \otimes I(\mathbf{x}). \quad (2)$$

At a given location $\mathbf{x} = \mathbf{b}$ for a given resolution (a), shape anisotropy (σ) and orientation (θ), the wavelet coefficient $C_I(a, \mathbf{x}, \sigma, \theta)$ is a local indicator of the match between the filter and the local content of the image. The significance of wavelet coefficients can easily be visualized in one dimension (Figure 2): (1) the wavelet having zero mean, the convolution between the given analyzing wavelet $\psi(a, \mathbf{x}, \sigma, \theta)$ localized in $\mathbf{x} = \mathbf{b}$ and a constant signal $I(\mathbf{x})$ produces null coefficients (Figure 2a); (2) negative coefficients underline the edge of the entities (Figure 2b); (3) small coefficients reflect a poor match between the given analyzing wavelet and the image (Figures 2c and 2d); and (4) maximum coefficients point out the best match with respect to the resolution, location, shape ratio, and orientation between the wavelets and the local content of the image (Figures 2e and 2f).

[10] A given wavelet is therefore a local and directional anisotropic filter that detects only structures having the

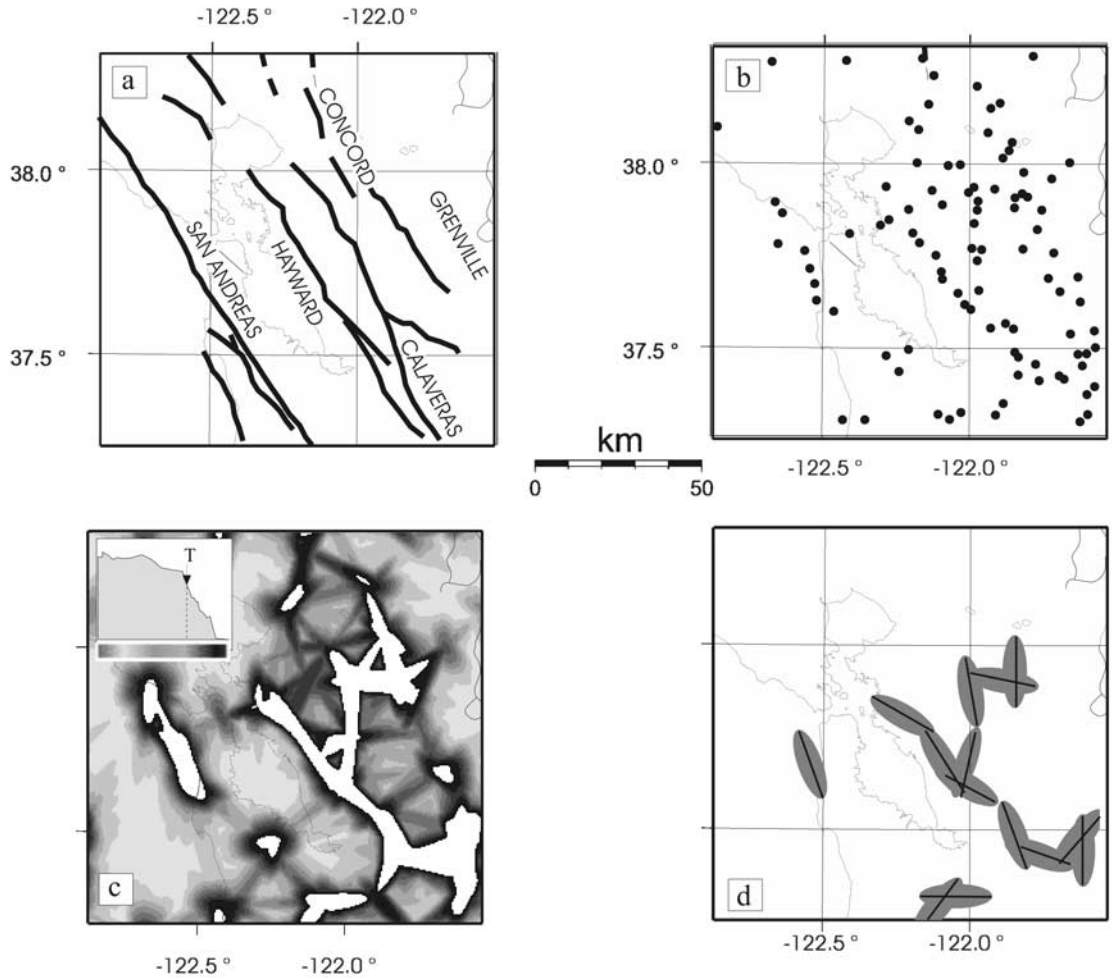

Figure 4. (a) Mapped faults from *Castillo and Ellsworth* [1993]. (b) Map of the 100 randomly selected epicenters (data from NCEDC, 1 January 1980 to 31 December 1997). (c) NOAWC map obtained for a resolution equal to the mean estimated error on location (a = 8 pixels ~4 km). Low coefficients are white; high coefficients are black. Long axis of the wavelets associated with the selected local maxima (T = 0.56) is plotted (thin line). (d) Detected structures with their incertitude envelope. The seismically active parts of the San Andreas, Calaveras, Hayward, Concord, and Greenville faults are again detected. E-W and N-S alignments have also been evidenced and correspond to extra lines in respect to mapped faults.

same geometrical parameters (Figure 1). In practice, for a given spatial resolution (a), a complete and objective detection of all structures requires in each point (**b**) the application of a range of filters each having a unique combination of (θ, σ) values [*Gaillot et al.*, 1997].

4. NOAWC Method

[11] The above procedure generates a very large number of wavelet coefficients. An image size of $N * N$ pixels generates $4N^2$ number of figures to handle ($N \times N$ figures for the a, σ, θ and wavelet coefficient dimension). To simplify their analysis, we developed the Normalized Optimized Anisotropic Wavelet Coefficient (NOAWC) method [*Darrozes et al.*, 1997] on the basis of the algorithms of *Ouillon et al.* [1995, 1996]. According to the wavelet coefficient properties (Figure 2) the filter that best describes the structure of an image, at each point, is characterized by a high coefficient (local maximum). So, for a given spatial resolution (a) the NOAWC method selects, for each point (**b**) of the image, among all the possible wavelets defined by (θ, σ) set, the optimum filter, i.e., the wavelet producing the highest local coefficient. In the resulting map, called NOAWC map, local maxima correspond to the center of mass of detected features [*Gaillot et al.*, 1997].

[12] Consequently, the frequency distribution histograms (logarithmic scale) of the wavelet coefficients of the NOAWC maps are systematically characterized by a kink between the few high coefficients and the numerous lower coefficients (Figure 2g). The local maxima superior to this threshold value (T in Figure 2g) are selected, and the corresponding wavelet parameters (resolution (a), location (**b**), length (σa) and orientation (θ)) are extracted. From the latter parameters of the wavelets the detected objects are represented by ellipses of width = (a), location, (**x** = **b**), length = (σa), and orientation (θ) (Figure 1). For conven-

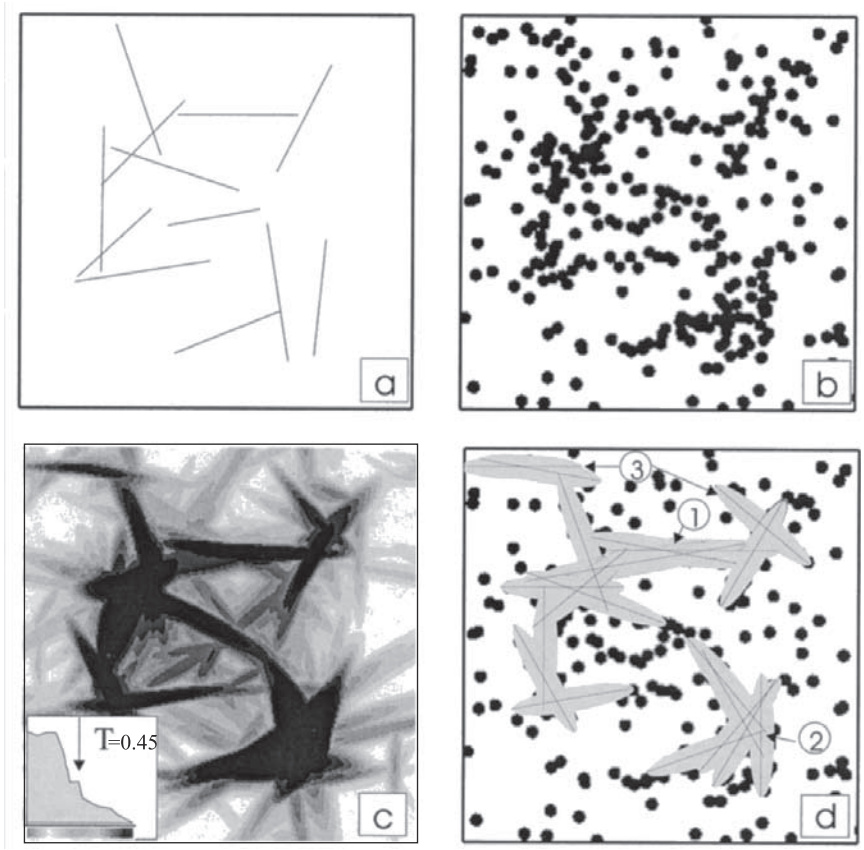

Figure 5. Illustration of examples of artifacts in the detection. (a) Randomly constructed structures (12) distributed in a 256 × 256 km area. (b) Spatial distribution of points (300). Fifty percent of the points are randomly located, and 50% of the points are distributed along the 12 structures. The latter are randomly perturbed with a maximum distance of 10 km. (c) NOAWC map obtained from a resolution equal to the mean error on the location (10 km), an integration scale (σa) varying from 3 to 256 km and an azimuth (θ) varying from 0° to 180°. Extraction of the wavelets parameters superior to the threshold value deduced from the kink ($T = 0.45$) of the wavelet coefficient allows extraction of significant lineaments. (d) Plots of significant lineaments with their uncertainty envelope.

ience, the long axes of the ellipses are underlined in the produced map of the significant lineament.

5. Two-Dimensional Illustration: San Francisco Bay Area

[13] We illustrate the mathematical efficiency of bidimensional anisotropic wavelets on the epicentral data from the Northern California Earthquake Catalog (http://quake.geo.berkley.edu), provided by the Northern California Earthquake Data Center (NCEDC) with the contribution of the Northern California Seismic Network (NCSN, U.S. Geological Survey, Menlo Park). Our test concerns the 2288 $M \geq 2$ seismic events that have occurred between 1 January 1980 and 31 December 1997 in the San Francisco Bay area (121.53°W to 122.87°W, 37.25°N to 38.32°N) (Figure 3a). There several well-known vertical or subvertical faults or fault segments are marked by densely aligned epicenters (Hayward, Greenville, Concord faults, segment of San Andreas fault through the San Francisco peninsula, and central segment of the Calaveras fault [*Castillo and Ellsworth*, 1993]; see Figure 3b). The lengths of these seismic

Figure 6. (opposite) Synthetic examples of projection effects and error location. Capability of detection and characterization of the rupture plane in terms of its dimensions (length (L) and width (W)) and orientation (dip (Δ) and strike (Φ)) depends on the error location (Δe) and the bias in location (Δp) due to projection effects. The size of the box is s. $\Phi = 52°$. (a) $\Delta = 90°$, $\Delta e = 0$, $\Delta p = 0$; (b) $\Delta = 90°$, $\Delta e = s/10$, $\Delta p = 0$; (c) $\Delta \neq 90°$, $\Delta e = 0$, $\Delta p = s/10$; (d) $\Delta \neq 90°$, $\Delta e = s/10$, $\Delta p = s/10$; (e, f, g, and h) NOAWC maps with logarithmic frequency coefficient histograms corresponding to the situations displayed in Figures 6a, 6b, 6c, and 6d, respectively. The local maxima (in dark shading) correspond to the center of mass of the detected plane. The critical value (arrow) allows to extract the filters associated to the detected entity of resolution $a = s/10$. Shading scale ranges from 0 (white) to 1 (black). (i, j, k, and l) Selected wavelets (resolution $a = s/10$) and spatial distribution of points for the situations displayed in Figures 6a, 6b, 6c, and 6d, respectively. (m, n, o, and p) Detected structures and quantification for the situations displayed in Figures 6a, 6b, 6c, and 6d, respectively.

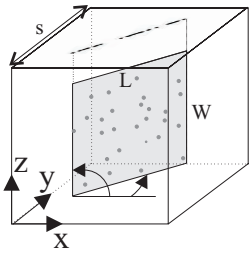

(a)

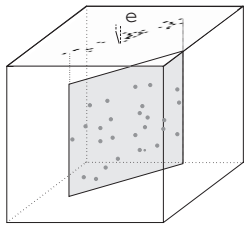

(b)

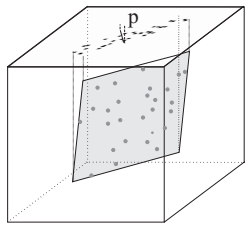

(c)

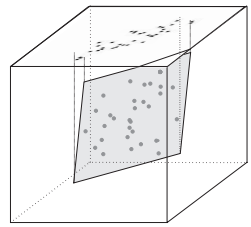

(d)

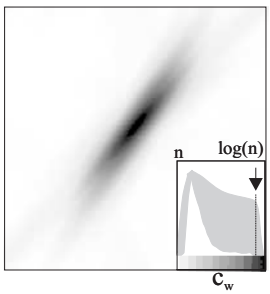

(e)

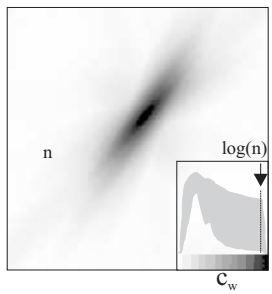

(f)

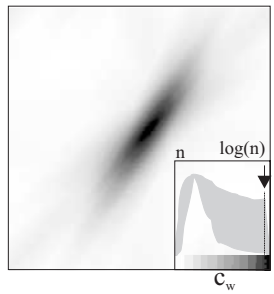

(g)

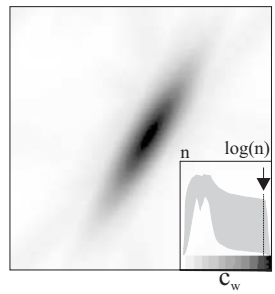

(h)

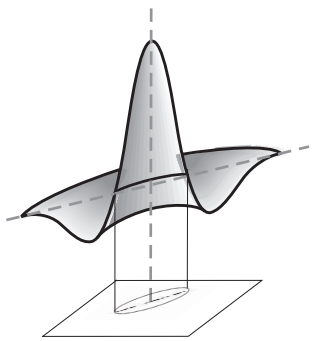

(i)

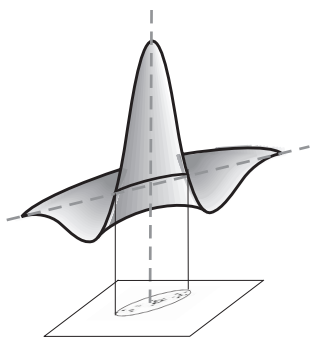

(j)

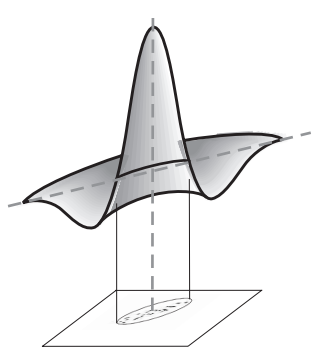

(k)

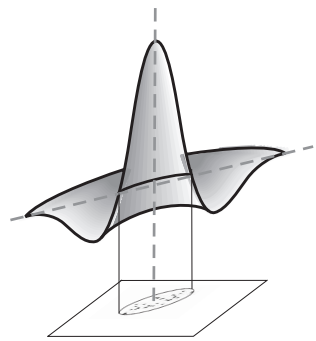

(l)

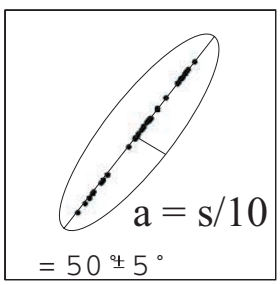

(m)

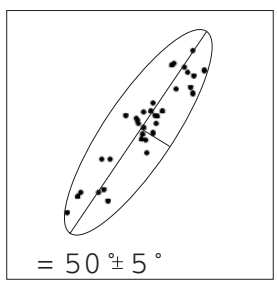

(n)

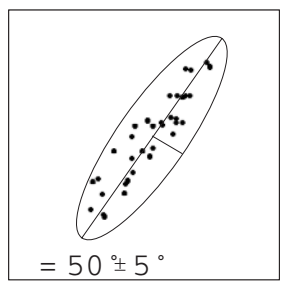

(o)

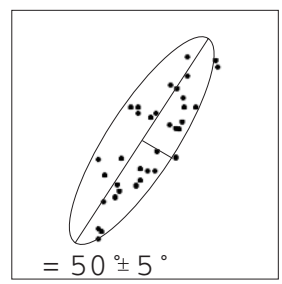

(p)

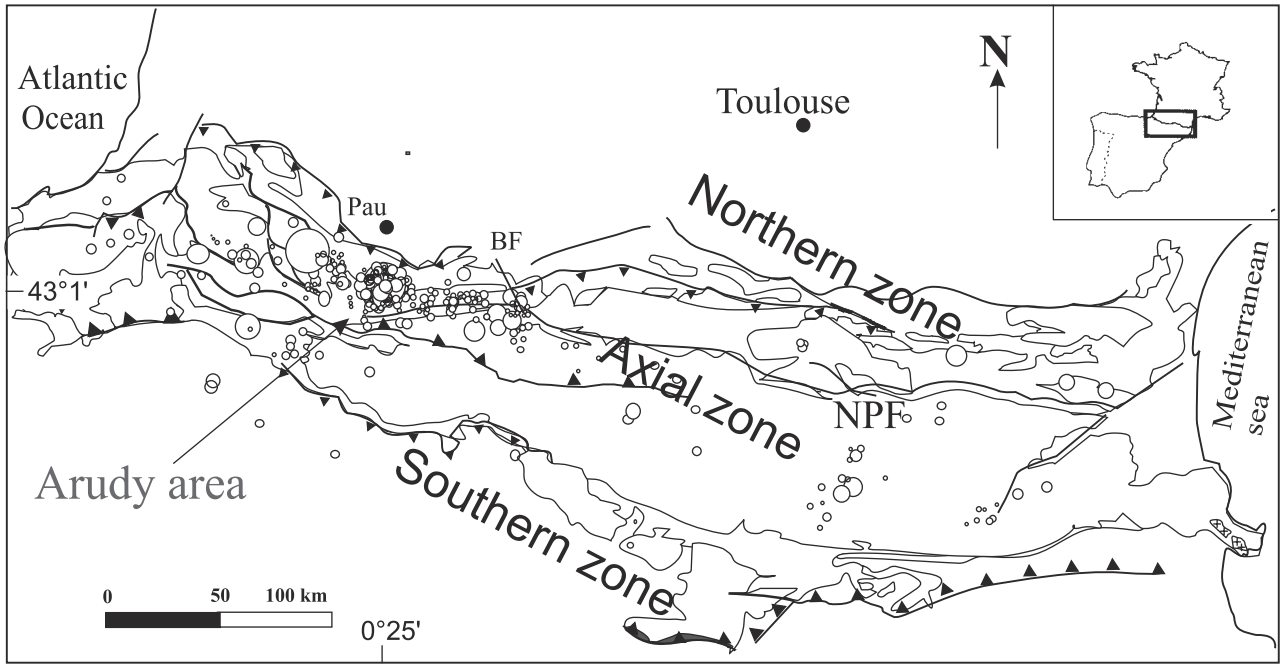

Figure 7. Structural sketch map of the Pyrenées. Circles, instrumental seismicity since 1963 [*Barnolas and Chiron*, 1996]. The Arudy earthquake epicentral zone is shown. NPF, North Pyrenean Fault; BF, Bigorre Fault.

features, within the study area, are ~40 km (except the Hayward fault, which exceeds 80 km). Because of the subverticality of the above mentioned structures, epicentral examination is used to illustrate wavelet efficiency to detect alignments. The NOAWC method is applied to these 2228 epicenters sampled in a 256 × 256 pixel grid covering ~14,500 km^2 (Figure 3b). For a set of wavelets having a spatial resolution equal to a = 8 pixels (~4 km), an integration scale (σa) from 3 to 256 pixels in steps of a/2 pixels and an azimuth (θ) varying from 0° to 180° in steps of 10°. The results are presented in Figure 3c. With an extraction of the wavelet parameters associated to wavelet coefficients greater than the threshold value $T \approx 0.60$ (Figure 3c), the San Andreas (through the San Francisco peninsula), Hayward, Calaveras, Concord, and Greenville faults are recovered by the NOAWC method (compare Figures 3c and 3b).

[14] In order to strengthen the relevance of our test and obtain a very sparse distribution of points, 100 events are randomly selected among the initial set of 2288 epicenters. The NOAWC method is applied to these 100 epicenters sampled in a 256 × 256 pixel grid covering ~14,500 km^2 (Figures 4a and 4b). The results for the same set of wavelets are presented in Figure 4b. With an extraction of the wavelet parameters associated to wavelet coefficients greater than the threshold value T = 0.56 (Figure 4c), the San Andreas (through the San Francisco peninsula), Hayward, Calaveras, Concord, and Greenville faults are mostly recovered by the NOAWC method (compare Figures 4d and 4a). Despite unfavorable conditions, the NOAWC method seems to be efficient for underlining significant clusters of seismic events regardless of their location, size, shape, and orientation. At this point, the analysis is purely mathematical. It is worth noting that some N-S alignments have also been evidenced (Figure 4d) and correspond to "extra lines" in respect to mapped faults. These extra lines could reveal unmapped tectonic features or could have a purely mathematical origin associated to localization error, effects of projection, or detection artifacts. Examples of such artifacts in the detection are discussed here under on a synthetic example.

[15] The main features of the synthetic data set are a 256 × 256 km area containing ~300 points, 50% of the points are randomly located, and 50% of the points are distributed along 12 lines having random orientations and locations (Figure 5). In addition, these points are randomly perturbed within a maximum distance of 10 km (Figures 5a and 5b). This simulates situations when points usually do not perfectly fall onto lines. As for the previous example, the analysis is performed with a resolution equal to the mean error on the location (10 km), an integration scale (σa) varying from 3 to 256 km in steps of 5 km and an azimuth (θ) varying from 0° to 180° in steps of 10°. Extraction of the wavelets parameters superior to the threshold value deduced from the kink (T = 0.45) of the wavelet coefficient histogram (Figure 5c) allows to extract significant lineaments (Figure 5d).

[16] Among these lineaments, extra lines of type 1 are associated with bowtie features resulting from multiple detection due to an oversampling in the method. This kind of artifact is removed by a visual inspection or an additional test applied after the NOAWC analysis. The type 2 of extra lines is characterized by zones of high density of points where many lines intersect. The type 3 extra lines are caused by significant alignments of random points. This mathematical approach, like all the methods of spatial analysis of seismic events, has its own limitations. As a common rule, interpretation of these mathematical results requires con-

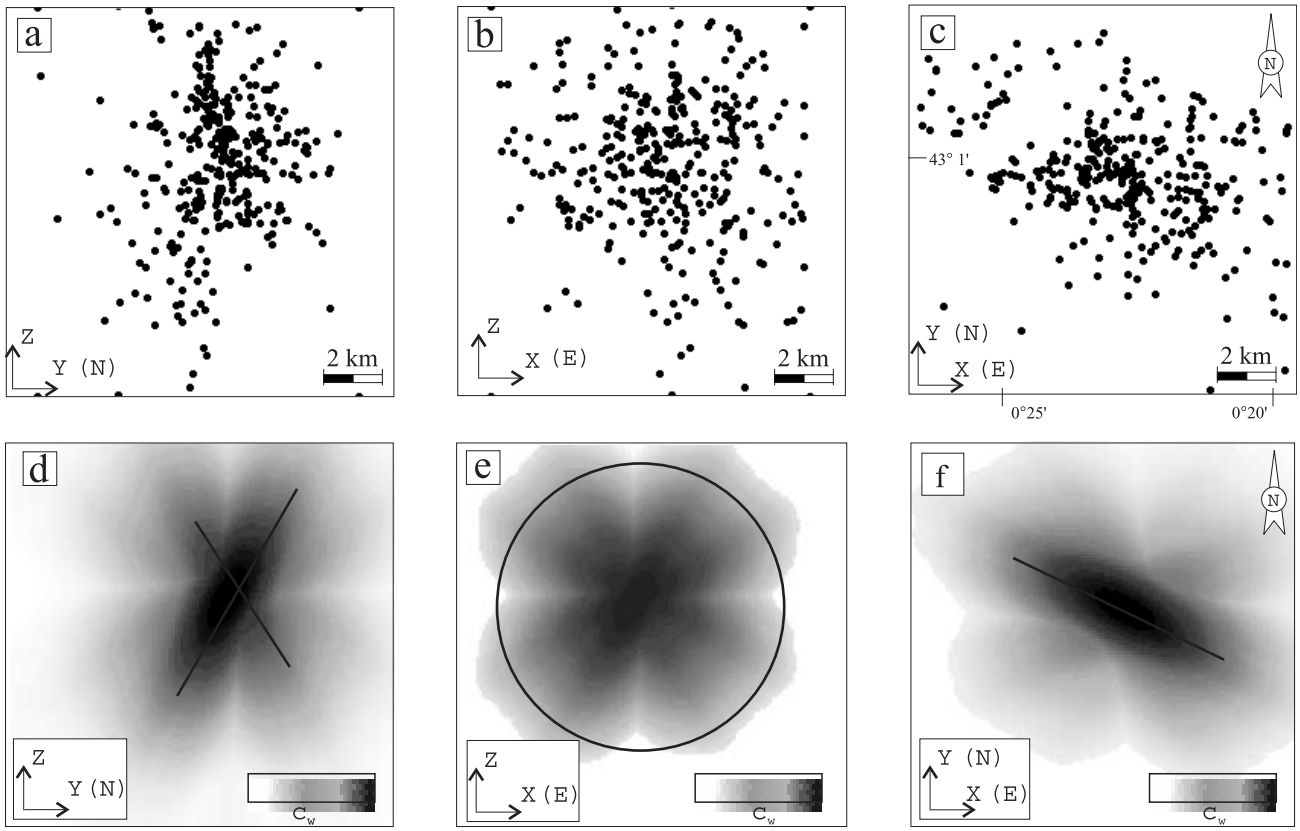

Figure 8. Results of large-scale analysis (*X*, east; *Y*, north; *Z*, depth axis). (a) Spatial distribution of seismic events projected onto the *YZ* section; (b) spatial distribution of seismic events projected onto the *XZ* section; (c) spatial distribution of seismic events projected onto the *XY* epicentral map; (d) *YZ* section, (e) *XZ* section, and (f) *XY* section NOAWC maps allowing deduction of the large-scale structural coherency of the inferred rupture zone and then selection of 2-D optimal sections for small-scale analysis.

frontation with geological and geophysical arguments such as local focal mechanisms and structural and geomorphological markers. So the mathematical results obtained by the NOAWC method are objective local guides for further investigations. The main advantage of the NOAWC method is that it makes the integration of complementary data sets easier by proposing a possible geometrical pattern.

[17] The ultimate objective of the technique is to detect lineaments in three dimensions, i.e., based on earthquake foci. Such an analysis is, however, difficult to handle with 3-D anisotropic wavelets due to the number of coefficients which induces a rather long time of computation and difficulties of visualization of the results (work in progress). As a first step toward this goal, we will reduce the dimensionality of the problem by projecting a 3-D foci distribution into 2-D sections of optimal azimuth and dip. This step has several shortcomings that we try to appraise in section 6.

6. NOAWC Method and Hypocentral Distribution of Seismic Events

[18] After having demonstrated the efficiency and limitations of the NOAWC method in two-dimensional sections, we have to consider that the geometry of rupture planes is a 3-D problem, taking into account their dimension (length (L) minus width (W)) and orientation (dip (Δ) minus strike (Φ)) that depend on the structural complexity [*Kanamori and Boschi*, 1983]. Reconstruction of such 3-D objects from 2-D sections requires minimization of the effects of projection of hypocenters (Δp). In addition, possible errors in the location of seismic events (Δe) have to be taken into account. We first used synthetic data to examine the effects of these errors and bias on the NOAWC method.

6.1. Synthetic Data

[19] The detection of the trace of a plane for four different test cases is illustrated in Figure 6. The first, and most favorable case, is characterized by a vertical plane ($\Delta = 90°$, $\Delta p = 0$) and null error location on hypocenters ($\Delta e = 0$) (Figure 6a). The second is still characterized by a vertical plane but the mean error location on epicenters, Δe is equal to 1/10 of the size (s) of the studied area (Figure 6b). The third is characterized by a dip (Δ) and width (W) of the plane generating a bias on the locations of epicenters, Δp also equal to s/10 (Figure 6c). The fourth is a combination of the second and the third cases with error location and projection effects (Figure 6d).

[20] The NOAWC maps obtained for a set of wavelets having a spatial resolution (a) equal to s/10, a shape ratio (σ) varying from 3 to 10 in steps of 0.5 and an azimuth (θ) varying from 0° to 180° in steps of 10° are shown in

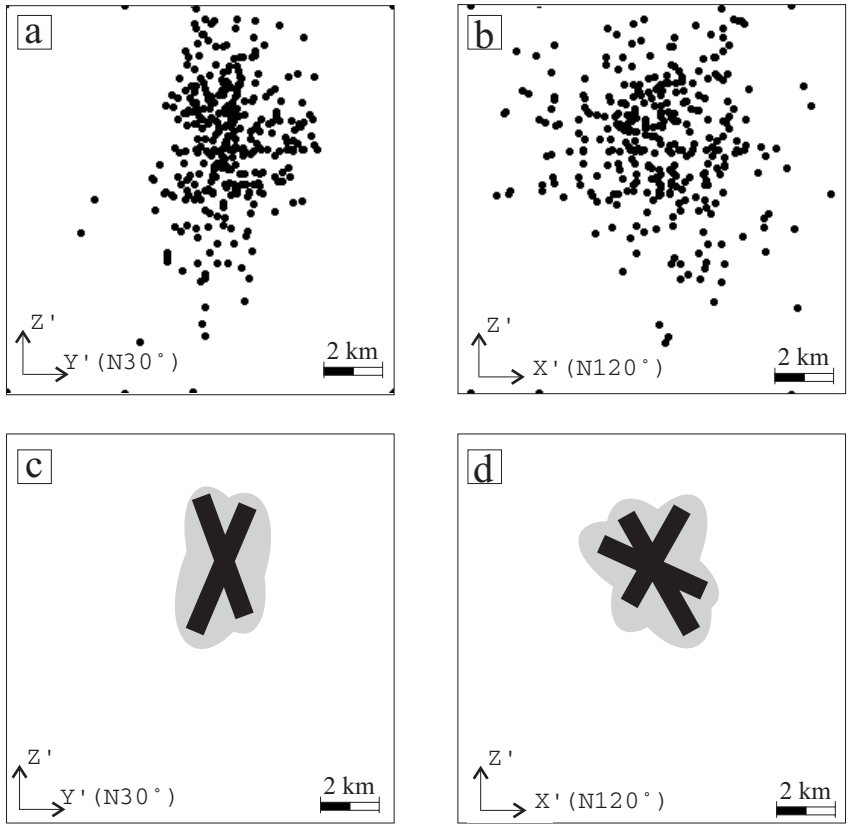

Figure 9. Small-scale analysis of the optimum $Y'Z'$ and $X'Z'$ sections (X' = N120°, Y' = N30°, Z' is depth axis). (a) Spatial distribution of seismic events projected onto the optimum $Y'Z'$ section; (b) spatial distribution of seismic events projected onto the optimum $X'Z'$ section; (c) detected structures in the optimum $Y'Z'$ section; and (d) detected structures in the optimum $X'Z'$ section. The two subvertical orientations evidenced in the $Y'Z'$ section and the isotropic pattern evidenced in the $X'Z'$ confirm the subverticality of the rupture zone.

Figures 6e–6h. The frequency wavelet coefficient histograms are also given in the lower right-hand corner. The slope break within the histograms (marked by an arrow) allows selection of the wavelet parameters associated with the highest local maxima, i.e., those that reflect significant structures at the given resolution.

[21] For a spatial resolution of the wavelet filter (a) equal to the maximum uncertainty on the location of the epicenters (s/10) and if the effects of projection are smaller than this uncertainty, the detected structure depends solely on the shape of the analyzed cluster (Figures 6i–6l). The NOAWC method thus provides an efficient method of detection and quantification of the significant structures (Figures 6m–6p). For all cases, the interpretation depends only on the uncertainty on the location of epicenters.

[22] A theoretical method could include the determination of a system of three perpendicular planes with arbitrary orientation on which the data would be adequately projected. However, for a given seismic zone the optimum configuration is controlled by the anisotropic distribution of hypocenters caused by large-scale structural coherency. Therefore our approach is, first, to perform a large-scale analysis. This preliminary computation enables us to determine the anisotropy of an inferred rupture zone from which three optimal perpendicular sections are deduced, hence allowing a small-scale analysis. Note that this approach does not require any geological assumptions.

6.2. Application: The M = 5.1 Arudy Earthquake Sequence

6.2.1. Seismic Data

[23] We now illustrate an application of the NOAWC method to the aftershock sequence of the 1980 Arudy earthquake in the Western French Pyrenees [*Gagnepain-Beyneix et al.*, 1982]. The main shock (M = 5.1) occurred a few tens of kilometers south of the city of Pau (latitude 43°4.21′N, longitude 0°24.59′W) at a depth of 4 ± 2 km (Figure 7) [see *Barnolas and Chiron*, 1996].

[24] We use data recorded by the permanent seismic network of Arette set up in 1978 by the Institut de Physique du Globe de Paris. The localization of $M \geq 1.5$ events are determined on the basis of three layers/one-dimensional velocity model [*Gagnepain-Beyneix et al.*, 1982]. For the selected events (N = 332), the uncertainties are estimated to be <800 m for the epicenters and <2 km for depths based on the *Gagnepain-Beyneix et al.* [1982] data set.

6.2.2. Large-Scale Analysis

[25] The first step, as mentioned above, consists of a large-scale analysis on three perpendicular sections in order to determine the optimal configuration that minimizes the

effects of projection. The spatial distribution of the seismic events covers an area of 13.3 × 13.3 km. It is presented in the *YZ*, *XZ*, and *XY* sections defined by the geographic coordinate system, i.e., *X* = east, *Y* = north, and *Z* is positive downward. Three binary images (256 × 256 pixel) are determined (Figures 8a, 8b and 8c, in which each pixel corresponds approximately to a 52 × 52 m square.

[26] To reduce the edge effects stemming from the periodization of both signal and wavelet, as recommended by *Ouillon et al.* [1995, 1996], the images, defined initially in a 256 × 256 pixels square, are embedded in a larger empty square of size 512 × 512 pixels. The NOAWC maps obtained from wavelets having a spatial resolution (*a*) equal to 64 pixels (1/4 of the zone of interest), a shape anisotropy (σ) varying from 1 to 4 in steps of 0.5 and an azimuth (θ) varying from 0° to 180° in steps of 10°, are presented in Figures 8d, 8e and 8f. Combining the three sections allows reconstruction of the large-scale geometry of the inferred rupture zone of the Arudy earthquake. The two orientations at 70° ± 5° and 110° ± 5° in the *YZ* section (Figure 8d), the isotropic pattern (altered by the diagonals of the image) of the *XZ* section (Figure 8e), and the main orientation at N120° in the *XY*, or epicentral, section (Figure 8f) reveal that the rupture zone is subvertical and strikes about N120°. The optimum configuration is thus obtained for X' parallel to N120°, Y' parallel to N30°, and Z' vertical.

6.2.3. Small-Scale Analysis

[27] After projection onto the three optimum perpendicular sections, $Y'Z'$, $X'Z'$, and $X'Y'$, defined above (Figures 9a and 9b, and 10a) the wavelet analysis is performed with a scale parameter (*a*) equal to the mean uncertainty on the data (a = 8 pixels ≈ 416 m for X′Y′ section and a = 38 pixels ≈ 1976 m for $X'Z'$ and $Y'Z'$ sections). The (σ, θ) set was chosen as in the previously discussed examples: the integration scale (σa) is ranging from 3a to 256 pixels by step of a/2 and the azimuth (θ) is varying from 0° to 180° in steps of 10°.

[28] The $Y'Z'$ and $X'Z'$ sections (Figures 9c and 9d) confirm the subverticality ($70° \leq \Delta \leq 90°$) of the rupture planes at a small scale. The subverticality of the rupture planes allows restriction of the analysis to the $X'Y'$ (or epicentral) section, in which localization uncertainties are the lowest. For convenience, results are shown in the geographic frame rather than in the $X'Y'$ frame.

[29] NOAWC map and histogram of wavelet coefficients (minimun value of 0.0, maximun value of 0.62) are given in Figure 10b. Extraction of the wavelet parameters associated to local maxima higher than the threshold value T (T = 0.42) interactively chosen from the kink of the wavelet coefficient histogram leads to the "lineament map" (Figure 10c). All the detected lineaments correspond to extra lines in respect to mapped faults of the same area (Figure 10d). In order to reject "mathematical extra lines" we plot the results obtained for the long ($\lambda > 4125$ m), medium ($2812 \text{ m} \leq \lambda \leq 3937$ m), and short ($1125 \text{ m} \leq \lambda \leq 2625$ m) wavelengths (Figures 10e–10g). At long wavelengths the three detected lineaments underline two possible subvertical

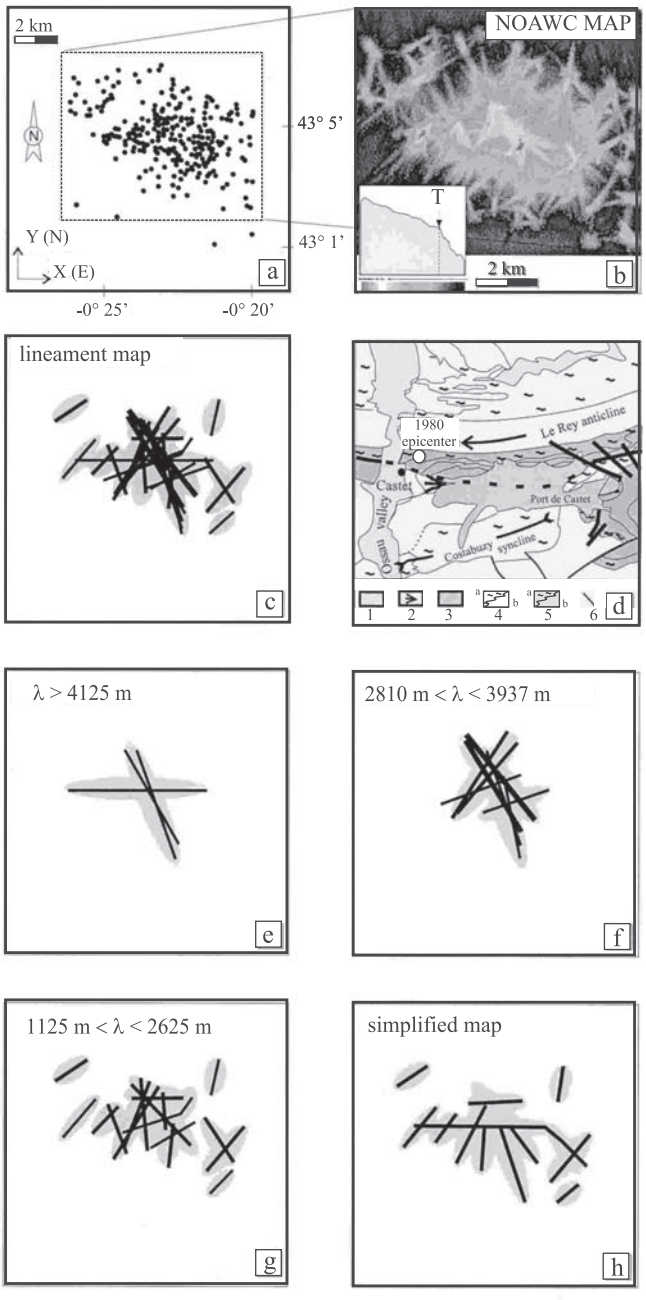

Figure 10. (opposite) Detailed small-scale analysis of the optimum $X'Y'$ section (X' = N120°, Y' = N30°). For convenience, results are presented in the *XY* frame. (a) Epicentral distribution of seismic events projected onto the *XY* section, (b) NOAWC map and wavelet coefficient histogram (T = 0.42), (c) lineament map obtained from the wavelet parameters associated to coefficients higher than the threshold value *T*, (d) structural sketch map of the studied area. 1, Quaternary alluvions; 2, late glacial dejection cones; 3, Würmian morainic materials; 4, Lower Cretaceous a, marls, and b, limestone; 5, Jurassic a, marls, and b, limestones; and 6, major faults. Mapped faults are from *Grasso* [1983]; (e) detected structures at long wavelengths ($\lambda \geq 4125$ m, light shading); (f) detected structures at medium wavelengths ($2812 \text{ m} \leq \lambda \leq 3937$ m, shaded); (g) detected structures at small wavelengths ($1125 \text{ m} \leq \lambda \leq 2625$ m, dark shading); and (h) simplified epicentral map with uncertainty envelopes (shaded) equal to ±0.4 km.

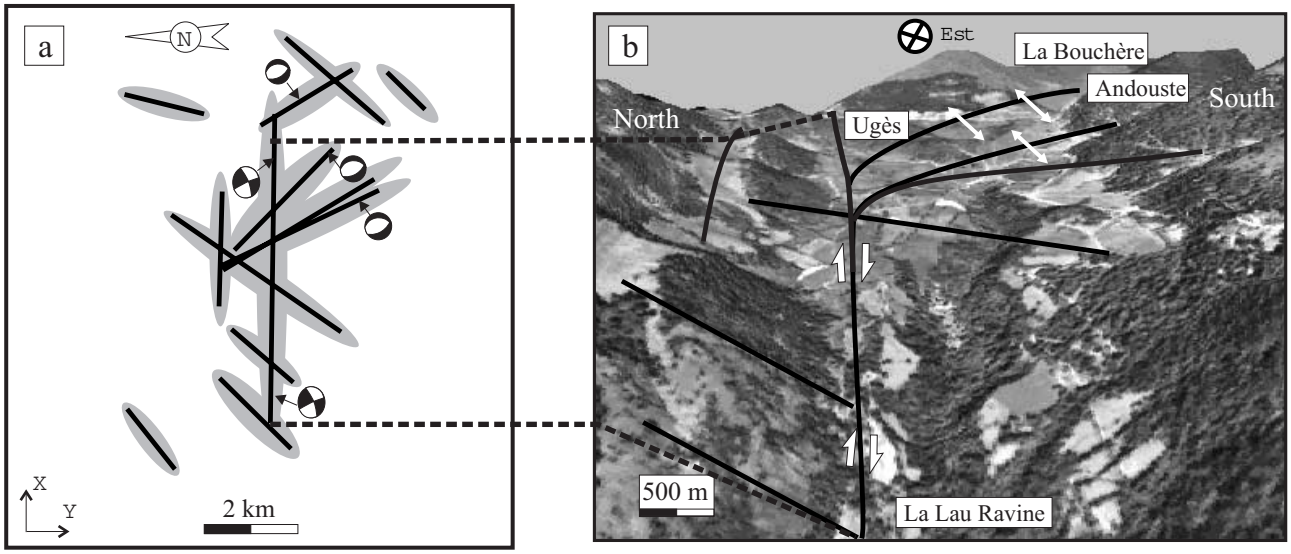

Figure 11. Reconstructed structural geometry and interpretation. (a) Combination of the simple epicentral map and fault plane solutions. This structural pattern could be integrated in a local model which takes the form of an ''horsetail'' termination of an E-W and subvertical dextral strike-slip fault [*Darrozes et al.*, 1998]. (b) Combination of the reconstructed structural pattern and a digital elevation model (DEM). Note the good spatial correlation between the detected active rupture planes and the main Würmian glacier valleys.

rupture planes striking E-W and ~N140°, respectively (Figure 10e). At intermediate wavelengths, interpretation is problematic due to a strong concentration of seismic events near central area (Figure 10f). At small wavelengths, main ~N150° and ~N40° central planes and the strong concentration of epicenters in the central zone are again detected. Five isolated planes oriented ~N40° are well defined away from the center. This pattern is completed by two lineaments at ~N10° and ~N150° (Figure 10g). Because of the uncertitude on the location of the seismic events and possible artifact on the detection, the most probable lineaments (i.e., lineaments able to explain the shape of the lineament map) are (Figure 10h) at small scale the isolated N40°, N140°, and N10° lineaments; at large scale, the main E-W and N140° lineaments; and at intermediate scale the N140° and the N30°–N40° lineaments. This representation of possible active rupture planes, displayed with uncertainty envelopes (±0.4 km in the *XY* map), is called a lineament map and must be combined with complementary seismological and geomorphological data before any validation and interpretation.

6.2.4. Geological Validity of the Lineament Map

[30] The combination of the possible reconstructed segment geometry with the focal mechanisms helps to determine the active rupture planes (Figure 11a). Fault plane solutions characterized by subvertical E-W and N-S nodal planes are nearly all associated with strike-slip motion as the E-W rupture. Fault plane solutions characterized by NW-SE nodal planes are associated with normal motion as the NW-SE rupture. This structural pattern could be integrated in a local tectonic model which takes the form of a horsetail termination of an E-W subvertical dextral strike-slip fault [*Darrozes et al.*, 1998]. In addition, the ''simplified map'' has been combined with a digital elevation model (DEM) to confirm and precise the location of the rupture planes. The correlation between the detected active rupture planes and the main recent glacial morphologic markers [*Lajournade*, 1983] (Würmian, ~100 ka) (Figure 11b) is consistent with the proposed tectonic model of *Darrozes et al.* [1998].

[31] The horsetail termination model predicts the creation of a compressive zone to the north east and a tensional zone to the south east marked by a group of pure normal faults subparallel to the regional compression axis showing a decreasing angle when they come closer to the main strike-slip zone [e.g., *Segall and Pollard*, 1980; *Granier*, 1985]. Further, such a horsetail termination structure is known to result from a mechanical heterogeneity which hampers progression of the slip motion. This heterogeneity has already been evidenced by high-velocity contrast of the *P* seismic waves between 3 and 5.5 km at the eastern limit of the aftershocks zone (W0°20 of longitude) [*Grasso*, 1983; *Souriau and Granet*, 1995] and has been interpreted as a seismic barrier for the propagation of the 1980 aftershock sequence [*Grasso*, 1983].

[32] The outgrowth of the horsetail termination structure would result from the oblique collision between the western and eastern upper crustal domains. This oblique collision would have started at least since the anticlockwise rotation of the compression axis in the Oligocene [*Hervouët*, 1997]. The resulting motion is accommodated along an ancient E-W dextral strike-slip thrust zone.

[33] It is worth noting that the NE-SW faults evidenced by the NOAWC procedure cannot be explained by the horsetail model. They would behave as normal faults, as indicated by the geomorphological markers. These steeply dipping faults, more or less perpendicular to the regional NW-SE compression direction, may belong to areas where massive carbonates (now overlain by Würmian moraines)

initially under compression were relaxed in tension at the end of the aftershock sequence.

7. Conclusion

[34] Because the strong limitations of geological mapping of (1) surface exposure and (2) determination of fault plane solutions of seismic events to characterize fault planes, mathematical investigation of spatial distribution of seismic events is proposed. Using the local and multiscale properties of the wavelet transform, allowing the investigation of multidimensional signals without condition or hypothesis on their nature, we developed the NOAWC method. This method underlines concentration of seismic events along alignments which are either mapped faults or extra lines with respect to these faults. In the latter case, further investigations are required to discern purely mathematical lineaments from newly evidenced geological features that in turn reveal the complete geometry of the active rupture zone.

[35] The procedure is completely determined by the specification of several parameters: the spatial resolution equal to the mean error location in the given 2-D section of the seismic events and the threshold value which is interactively chosen from the slope break of the wavelet coefficient histogram. As shown by synthetic and real data, the implementation of wavelet filtering picks out the significant features linked to the seismically active rupture planes accounting for uncertainty in the location of the seismic events. As illustrated by the 1980 Arudy (M = 5.1, French Pyrenees) earthquake sequence, the method is part of a quantitative, objective, computer-assisted analyses of large bodies of data. Coupled with fault plane solutions of seismic events and geological mapping of fault surface exposure, when available, it provides key information for the reconstruction of the 3-D structural geometry of the rupture zone.

[36] **Acknowledgments.** We thank G. Marquis (EOST, Strasbourg) and M. Daignières (ISTEEM, Montpellier) for their valuable comments on the manuscript and the two reviewers.

References

Amorese, D., J.-L. Lagarde, and E. Laville, A point pattern analysis of the distribution of earthquake in normandy (France), *Bull. Seismol. Soc. Am.*, *89*, 742–749, 1999.

Antoine, J. P., P. Carette, and R. Murenzi, Image analysis with 2D continuous wavelet transform, *Signal Process.*, *31*, 241–272, 1993.

Barnolas, A., and J. C. Chiron, *Synthèse Géologique et Géophysique*, vol. 1, *Introduction*, Bur. de Rech. Géol. et Min., Orléans, France, 1996.

Bethoux, N., G. Ouillon, and M. Nicolas, The instrumental seismicity of the western Alps: Spatio-temporal patterns analysed with the wavelet transform, *Geophys. J. Int.*, *135*, 177–194, 1998.

Castillo, D. A., and W. L. Ellsworth, Seismotectonics of the San Andreas fault system between Point Arena and Cape Mendocino in northern California: Implications for the development and evolution of a young transform, *J. Geophys. Res.*, *98*, 6543–6560, 1993.

Chapman, C., C. A. Powell, G. Vlahovic, and M. S. Sibol, A statistical analysis of earthquake focal mechanisms and epicenter locations in the eastern Tennessee seismic zone, *Bull. Seismol. Soc. Am.*, *87*, 1522–1536, 1997.

Chui, C. K., *An Introduction to Wavelets*, 266 pp., Academic, San Diego, Calif., 1992.

Darrozes, J., P. Gaillot, M. de Saint Blanquat, and J.-L. Bouchez, Software for multi-scale image analysis: The normalised optimised anisotropic wavelet coefficient method, *Comput. Geosci.*, *23*, 889–895, 1997.

Darrozes, J., P. Gaillot, and P. Courjault-Radé, 2D propagation of a sequence of aftershocks combining anisotropic wavelet transform and GIS, *Phys. Chem. Earth*, *23*, 303–308, 1998.

Daubechies, I., *Ten Lectures on Wavelets, CBMS-NSF Reg. Conf. Ser. Appl. Math.*, vol. 61, 357 pp., Soc. of Ind. and Appl. Math., Philadelphia, Pa., 1992.

Eneva, M., and G. L. Pavlis, Application of pair analysis statistics to aftershocks of the 1984 Morgan Hill, California, earthquake, *J. Geophys. Res.*, *93*, 9113–9125, 1988.

Escalera, E., and H. T. MacGillivray, Topology in galaxy distributions: Method for a multi-scale analysis: A use of the wavelet transform, *Astron. Astrophys.*, *298*, 1–21, 1995.

Fehler, M., L. House, and H. Kaieda, Determining planes along which earthquakes occur: Method and application to earthquake accompanying hydraulic fracturing, *J. Geophys. Res.*, *92*, 9407–9414, 1987.

Frohlich, C., and S. D. Davis, Single-link cluster analysis as a method to evaluate spatial and temporal properties of earthquake catalogues, *Geophys. J. Int.*, *100*, 19–32, 1990.

Gagnepain-Beyneix, J., H. Haessler, and T. Modiano, The Pyrenean earthquake of February 29, 1980: An example of complex faulting, *Tectonophysics*, *85*, 273–290, 1982.

Gaillot, P., J. Darrozes, G. Ouillon, and M. de Saint Blanquat, The normalised optimised anisotropic wavelet coefficient (NOAWC) method: An image processing tool for multi-scale analysis of rock fabric, *Geophys. Res. Lett.*, *24*, 1819–1822, 1997.

Granier, T., Origin, damping, and fault pattern of development of faults in granite, *Tectonics*, *4*, 721–737, 1985.

Grasso, J. R., Three dimensional velocity image of a barrier associated with a moderate pyrenean earthquake, *Geophys. Res. Lett.*, *10*, 229–232, 1983.

Hagelberg, C., and J. Helland, Thin line detection in meteorological radar images using wavelet transforms, *J. Atmos. Oceanic Technol.*, *12*, 633–642, 1995.

Hauksson, E., L. M. Jones, and K. Hutton, The 1994 Northridge earthquake sequence in California: Seismological and tectonic aspects, *J. Geophys. Res.*, *100*, 12,335–12,355, 1995.

Hervouët, Y., Deformations alpines, inversion tectonique négative et karstogène, exemple de la Pierre Saint-Martin (Pyrénées Atlantiques, France), *Bull. Soc. Géol. Fr.*, *168*, 663–674, 1997.

Jones, R. H., and R. C. Stewart, A method for determining significant structures in a cloud of earthquakes, *J. Geophys. Res.*, *102*, 8245–8254, 1997.

Kagan, Y. Y., Spatial distribution of earthquakes: The three points moment function, *Geophys. J. R. Astron. Soc.*, *67*, 697–717, 1981a.

Kagan, Y. Y., Spatial distribution of earthquakes: The four points moment function, *Geophys. J. R. Astron. Soc.*, *67*, 719–733, 1981b.

Kagan, Y. Y., and L. Knopoff, Statistical search for non-random features of the seismicity of strong earthquakes, *Phys. Earth Planet. Inter.*, *12*, 291–318, 1976.

Kagan, Y., and L. Knopoff, Statistical study of the occurrence of shallow earthquakes, *Geophys. J. R. Astron. Soc.*, *55*, 67–86, 1978.

Kagan, Y., and L. Knoppoff, Stochastic synthesis of earthquake catalogues, *J. Geophys. Res.*, *86*, 2853–2862, 1981.

Kanamori, H., and E. Boschi, *Earthquakes, Observation, Theory and Interpretation*, edited by H. Kanamori and E. Boschi, 596 pp., North-Holland, New York, 1983.

Lajournade, C., Géomorphologie glaciaire de la vallée de Castet (Vallée d'Ossau, Pyrénées Atlantiques), report, Geography Dep., Toulouse Univ., Toulouse, France, 1983.

Meyer, Y., and S. Roques, *Progress in Wavelet Analysis and Applications*, edited by Y. Meyer and S. Roques, 785 pp., Frontières, Paris, 1993.

Ouchi, T., and T. Uekawa, Statistical analysis of the spatial distribution of earthquakes: Variation of the spatial distribution of earthquakes before and after large earthquakes, *Phys. Earth Planet. Inter.*, *44*, 211–225, 1986.

Ouillon, G., D. Sornette, and C. Castaing, Organisation of joints and faults from 1 cm to 100 km scales revealed by optimized anisotropic wavelet coefficient method and multifractal analysis, *Nonlinear Processes Geophys.*, *2*, 158–177, 1995.

Ouillon, G., C. Castaing, and D. Sornette, Hierarchical geometry of faulting, *J. Geophys. Res.*, *101*, 5477–5487, 1996.

Prozorov, A. G., and A. M. Dziewonski, A method of studying variations in the clustering property of earthquakes: Application to the analysis of global seismicity, *J. Geophys. Res.*, *87*, 2829–2839, 1982.

Reasenberg, P., Second-order moment of central California seismicity, *J. Geophys. Res.*, *90*, 5479–5495, 1985.

Robertson, M. C., C. G. Sammis, M. Sahimi, and A. Martin, The 3D

spatial distribution of earthquakes in southern California with a percolation theory interpretation, *J. Geophys. Res.*, *100*, 609–620, 1995.

Segall, P., and D. Pollard, Mechanics of discontinuous faults, *J. Geophys. Res.*, *85*, 4337–4350, 1980.

Souriau, A., and M. Granet, A tomographic study of the litosphere beneath the Pyrenees from local and teleseismic data, *J. Geophys. Res.*, *100*, 18,117–18,134, 1995.

Suzuki, Z., and K. Suzuki, On space distribution function of earthquakes, *Sci. Rep. Tohoku Univ., 5th Ser. Geophys.*, *17*, 9–23, 1965.

Suzuki, Z., and K. Suzuki, Change in spatial distribution of earthquakes against hypocentral depth, *Sci. Rep. Tohoku Univ., 5th Ser. Geophys.*, *17*, 159–168, 1966.

Vere-Jones, D., Space-time correlations for microearthquakes—A pilot study, *Adv. Appl. Probab., Suppl.*, *10*, 73–87, 1978.

D. Amorese, UMR CNRS 6143 "M2C", Centre de Géomorphologie, Université de Caen, F-14032Caen Cedex, France. (amorese@geos-unicaen.fr)

P. Courjault-Radé and J. Darrozes, UMR 5563, CNRS, Observatoire Midi Pyrénées, Université Paul Sabatier, 38 rue des 36 ponts, F-31400 Toulouse, France. (pierrecr@lmtg.ups-tlse.fr; darrozes@lmt.ups-tlse.fr)

P. Gaillot, UMR 5568, CNRS, Laboratoire de Géophysique et Hydrodynamique de Forage, Université de Montpellier 2, F-34095 Montpellier Cedex, France. (gaillot@dstu.univ-montp2.fr)